Article

Plasma Ag-Modified α-Fe$_2$O$_3$/g-C$_3$N$_4$ Self-Assembled S-Scheme Heterojunctions with Enhanced Photothermal-Photocatalytic-Fenton Performances

Yawei Xiao [1], Bo Yao [1], Zhezhe Wang [1], Ting Chen [2,*], Xuechun Xiao [1,*] and Yude Wang [3,*]

[1] National Center for International Research on Photoelectric and Energy Materials, School of Materials and Energy, Yunnan University, Kunming 650504, China

[2] Institute of Materials Science & Devices, School of Materials Science and Engineering, Suzhou University of Science and Technology, Suzhou 215009, China

[3] Yunnan Key Laboratory of Carbon Neutrality and Green Low-Carbon Technologies, Yunnan University, Kunming 650504, China

* Correspondence: chenting@mail.usts.edu.cn (T.C.); xchxiao@ynu.edu.cn (X.X.); ydwang@ynu.edu.cn (Y.W.)

Abstract: Low spectral utilization and charge carrier compounding limit the application of photocatalysis in energy conversion and environmental purification, and the rational construction of heterojunction is a promising strategy to break this bottleneck. Herein, we prepared surface-engineered plasma Ag-modified α-Fe$_2$O$_3$/g-C$_3$N$_4$ S-Scheme heterojunction photothermal catalysts by electrostatic self-assembly and light deposition strategy. The local surface plasmon resonance effect induced by Ag nanoparticles broadens the spectral response region and produces significant photothermal effects. The temperature of Ag/α-Fe$_2$O$_3$/g-C$_3$N$_4$ powder is increased to 173 °C with irradiation for 90 s, ~3.2 times higher than that of the original g-C$_3$N$_4$. The formation of 2D/2D structured S-Scheme heterojunction promotes rapid electron-hole transfer and spatial separation. Ternary heterojunction construction leads to significant enhancement of photocatalytic performance of Ag/α-Fe$_2$O$_3$/g-C$_3$N$_4$, the H$_2$ photocatalytic generation rate up to 3125.62 μmol g^{-1} h^{-1}, which is eight times higher than original g-C$_3$N$_4$, and the photocatalytic degradation rate of tetracycline to reach 93.6%. This thermally assisted photocatalysis strategy improves the spectral utilization of conventional photocatalytic processes and provides new ideas for the practical application of photocatalysis in energy conversion and environmental purification.

Keywords: S-Scheme heterojunction; photothermal effect; 2D/2D structure; surface plasmon resonance; photocatalytic-Fenton

1. Introduction

Energy crisis and environmental pollution have become urgent problems to be solved, and photocatalytic technology is a green way to tackle them [1–4]. The core issue of photocatalysis is to increase the activity of the photocatalysts, and many semiconductor materials have been used in photocatalysis so far, such as TiO$_2$, CdS, MoSe$_2$, g-C$_3$N$_4$, and perovskite-type composite oxide. Among them, g-C$_3$N$_4$ is a novel nonmetallic polymer semiconductor, which has been widely used in photocatalysis because of its suitable forbidden bandwidth and tunable energy band structure [5–8]. The architecture of g-C$_3$N$_4$ is similar to that of graphene, and it has excellent thermal and chemical stability, which is attributed to the aromatic conjugated system formed by C-N heterocycles and van der Waals forces of interlayer interaction [9,10]. However, for a single g-C$_3$N$_4$ photocatalyst, the high exciton binding energy makes the photo-generated electrons and holes generated by photoexcitation easily complexed, and the oxidation capacity of the holes on its valence band is not sufficient to generate strongly oxidizing hydroxyl radicals, which is extremely unfavorable for photocatalytic reactions [11,12]. A new S-Scheme heterojunction was

proposed to provide a new direction for g-C_3N_4 modification recently. The selection of suitable semiconductors to construct S-Scheme heterojunctions with g-C_3N_4 can form higher conduction band (CB) positions or lower valence band (VB) positions to enhance the redox ability of g-C_3N_4. In addition, the hybridization will generate a new electronic structure, and the potential difference between the two sides of the heterojunction will form an internal electric field and energy band bending at the interface, which promotes photogenerated carrier migration and separation [13–15].

The pure g-C_3N_4 can only rely on its own photo-excited holes and oxygen-generated radicals generated by photogenerated electrons combined with oxygen to achieve the degradation of pollutants, which is not effective in the degradation of persistent organic pollutants [16–20]. The non-homogeneous Fenton reaction shows a high capacity for the removal of hard-to-degrade organic pollutants, and the photocatalytic-coupled Fenton system is one of the most promising approaches to address water pollution [21–25]. As a typical Fenton catalyst, α-Fe_2O_3 has been widely used in photocatalysis because of its suitable band gap, cost-effectiveness, and thermodynamic stability. Combining α-Fe_2O_3 with g-C_3N_4 to construct S-Scheme heterojunction photocatalytic-Fenton coupling system is a promising scheme to improve the photocatalytic activity of g-C_3N_4 [26,27]. The two-electron oxygen reduction reaction (ORR) in the photocatalytic system is capable of generating H_2O_2 without additional H_2O_2, and the photogenerated electrons capture dissolved oxygen in water and generate H_2O_2 near the catalyst, which in turn promotes the following chain reaction between Fe^{3+} and H_2O_2 to increase the concentration of hydroxyl radical ($\cdot OH$) in the system:

$$Fe^{2+} + H_2O_2 \rightarrow Fe^{3+} + \cdot OH + OH^- \tag{1}$$

$$Fe^{3+} + H_2O_2 \rightarrow Fe^{2+} + \cdot OOH + H^+ \tag{2}$$
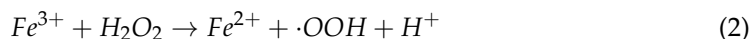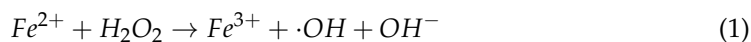
Moreover, as a narrow bandgap semiconductor, α-Fe_2O_3 can effectively broaden the spectral absorption interval of g-C_3N_4, improve the spectral utilization of sunlight, and enhance the photothermal conversion effect of the catalyst [28,29]. Therefore, the photocatalytic-Fenton coupling system composed of α-Fe_2O_3/g-C_3N_4 composites can further improve its photocatalytic performance in theory [30,31].

As a promising photocatalytic technique, surface plasmon resonance has received great attention in recent years [32–35]. Plasma photocatalysis can extend the absorption range of light through localized surface plasmon resonance (LSPR) [36–38]. LSPR of noble metal nanoparticles creates an enhanced surrounding local electric field that can linearly increase the concentration of photogenerated carriers. The effect of the enhanced electric field can also extend to the space charge layer of the adjacent semiconductors, increasing the concentration of photogenerated carriers near the semiconductor surface [39,40]. In addition, the Schottky barrier between the metal nanoparticles and the semiconductor can promote the transfer of the charge carriers to opposite directions, further injecting energetic (hot) electrons into the semiconductor, causing a much higher concentration of energetic electrons on the surface of the photocatalyst [41–43]. The energy of the oscillating electrons excited by plasma resonance can be decayed by non-radiative pathways, and the high-energy electrons are coupled to the phonon mode heating the metal lattice through electron-phonon scattering. This heat is eventually diffused into the environment by phonon-phonon relaxation, creating a local thermal effect at the catalyst interface, which speeds up the reaction rate on the catalyst surface [44,45]. In addition, the local electric field generated by LSPR of noble metals facilitates the polarized adsorption of reactant molecules on the surface of the photocatalytic material, which promotes the catalytic activity of the catalyst. Ag has been widely used in photocatalysis because of its cost advantage, abundant reserves, stable nature, and unique antibacterial properties. For instance, Xing et al. introduced silver nanoparticles into the catalytic systems of titanium dioxide and molybdenum sulfide, which showed enhanced light absorption and photocatalytic ac-

tivity [46,47]. Therefore, the introduction of silver nanoparticles is the preferred way to construct efficient photocatalytic materials.

In this work, Ag/α-Fe$_2$O$_3$/g-C$_3$N$_4$ ternary composite photocatalysts were prepared by electrostatic self-assembly and light deposition strategy. The construction of S-Scheme heterojunction in Ag/α-Fe$_2$O$_3$/g-C$_3$N$_4$ can effectively drive photogenerated carrier separation and transfer. Ag nanoparticles can expand the light absorption range, provide additional active sites, and also produce excellent photothermal effects through LSPR. The prepared Ag/α-Fe$_2$O$_3$/g-C$_3$N$_4$ shows much higher performance than pristine g-C$_3$N$_4$ for hydrogen production and degradation of tetracycline (TC). The special 2D/2D combination and charge carriers transfer pathway of Ag/α-Fe$_2$O$_3$/g-C$_3$N$_4$ were verified by detailed characterization, and the enhanced photothermal effect of Ag/α-Fe$_2$O$_3$/g-C$_3$N$_4$ ternary photocatalysts in both gas-phase and liquid-phase was also demonstrated by photothermal testing, then we proposed a synergistic photothermal-photocatalytic-Fenton catalytic mechanism. This work provides a new option for the design of cost-effective, highly active catalysts, as well as a potential way to solve the growing energy crisis and environmental pollution problems.

2. Experimental Section

The preparation process of Ag/α-Fe$_2$O$_3$/g-C$_3$N$_4$ ternary heterojunction photocatalyst is shown in Figure 1. First, the supramolecular precursors composed of melamine and cyanuric acid were calcined to obtain g-C$_3$N$_4$ ultrathin nanosheets, and hexagonal α-Fe$_2$O$_3$ nanosheets were prepared by one step hydrothermally. The zeta potentials of g-C$_3$N$_4$ and α-Fe$_2$O$_3$ were measured to be -23.9 mV and $+28.3$ mV, respectively (Figure S1). g-C$_3$N$_4$ and α-Fe$_2$O$_3$ were assembled into heterojunctions driven by electrostatic forces between positive and negative charges, and then Ag/α-Fe$_2$O$_3$/g-C$_3$N$_4$ was obtained by modifying Ag nanoparticles on the α-Fe$_2$O$_3$/g-C$_3$N$_4$ surface via light deposition process. The specific experimental parameters and test procedures are detailed in the supplemental material.
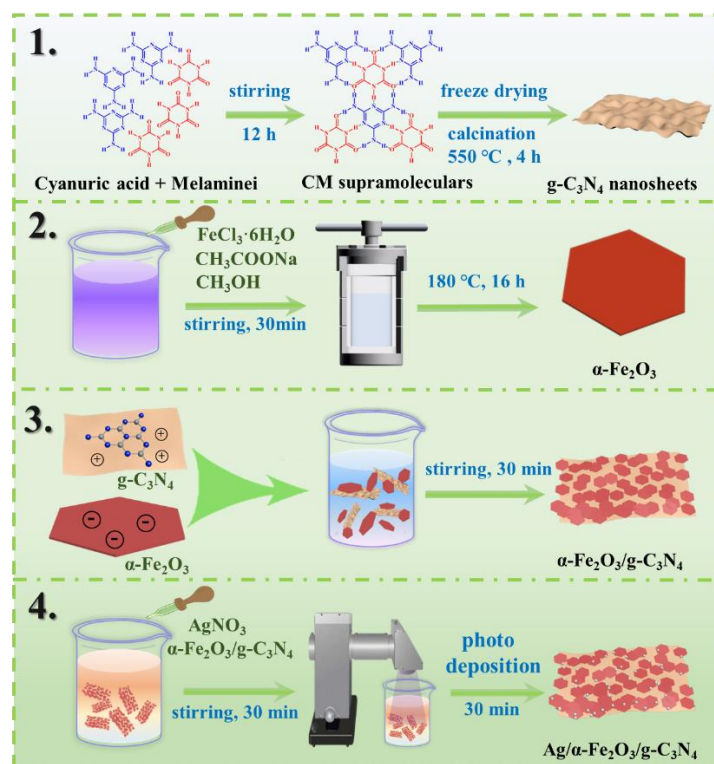

Figure 1. Scheme diagram of the preparation process of Ag/α-Fe$_2$O$_3$/g-C$_3$N$_4$ sandwich-like self-assembled S-Scheme heterojunction photocatalyst.

2.1. Preparation of g-C$_3$N$_4$ ultra-Thin Nanosheets

The bottom-up supramolecular self-assembly method was used to prepare g-C$_3$N$_4$ ultrathin nanosheets. In a typical synthesis process, 0.01 mol melamine and 0.01 mol cyanuric acid were dissolved in 50 mL of deionized water and stirred at room temperature for 12 h after being mixed. Subsequently, the white melamine-melamine supramolecules were centrifuged and freeze-dried for 24 h. Then, they were warmed up to 550 °C in a muffle furnace at a rate of 5 °C min^{-1} and kept for 4 h. The light-yellow 3D g-C$_3$N$_4$ was gained after cooling.

2.2. Preparation of Hexagonal α-Fe$_2$O$_3$ Nanosheets

Hexagonal α-Fe$_2$O$_3$ nanosheets were prepared by one-step solvothermal synthesis. In a typical synthesis, 2.0 mmol of FeCl$_3$·6H$_2$O was dissolved into a mixed solution of 20 mL ethanol and 1.4 mL water under vigorous magnetic stirring, and 1.6 g of sodium acetate was added after complete dissolution of FeCl$_3$·6H$_2$O and stirring was continued for 0.5 h. Subsequently, the homogeneous solution was transferred to a 50 mL Teflon-lined reactor sealed with a stainless-steel sheath and kept at 180 °C for 12 h. After cooling to room temperature, the resulting precipitate was rinsed several times with alternating deionized water and ethanol and dried overnight at 60 °C to obtain α-Fe$_2$O$_3$ hexagonal nanosheets.

2.3. Preparation of α-Fe$_2$O$_3$/g-C$_3$N$_4$ Heterojunction Photocatalyst

α-Fe$_2$O$_3$/g-C$_3$N$_4$ heterojunction photocatalysts were prepared by electrostatic self-assembly method. A total of 50 mg of g-C$_3$N$_4$ nanosheets were dispersed in 80 mL of deionized water. Then different amounts of α-Fe$_2$O$_3$ powder were taken and ultrasonically dispersed in 50 mL of deionized water, and the obtained α-Fe$_2$O$_3$ solution was added to the g-C$_3$N$_4$ nanosheet suspension under vigorous stirring, and a uniform suspension was obtained after slow stirring for 6 h. After the suspension is filtered, it is washed several times with deionized water and methanol. The obtained mixed powder was dried overnight in an oven at 60 °C to obtain α-Fe$_2$O$_3$/g-C$_3$N$_4$ heterojunction photocatalyst.

2.4. Preparation of Ag/α-Fe$_2$O$_3$/g-C$_3$N$_4$ Ternary Composite Photocatalyst

Ag quantum dots were deposited on the surface of α-Fe$_2$O$_3$/g-C$_3$N$_4$ using light deposition process. About 0.2 g of α-Fe$_2$O$_3$/g-C$_3$N$_4$ was added to 100 mL of deionized water and stirred for 30 min, then different volumes of AgNO$_3$ (0.1 M) solution were added and the mixed solution was irradiated with a 300 W xenon lamp for 30 min under stirring. Finally, the mixed solution was filtered, washed several times with deionized water, and dried in an oven at 50 °C to obtain the Ag/α-Fe$_2$O$_3$/g-C$_3$N$_4$ ternary product.

2.5. Experiment Characterizations

The X-ray diffractometer (XRD, Rigaku, Japan, λ = 1.5418 Å) was used to determine the phase structure of the prepared photocatalysts. The transmission electron microscope (TEM, JEM-2100, Japan) and scanning electron microscope (SEM, Nova nano SEM 450) were used to examine the microstructure of the photocatalysts, and the distribution of the elements was detected by TEM equipped with the energy dispersive spectrometer (EDS). X-ray photoelectron spectroscopy (XPS) was performed by a photoelectron spectrometer (Thermo ESCALAB 250Xi, USA). The ultraviolet-visible (UV-Vis) diffuse reflectance spectra of the catalysts were measured by a spectrophotometer (UV-2600i, Shimadzu, Japan). Photoluminescence (PL) spectra of the photocatalysts were measured with an FLS 1000 fluorescence spectrophotometer (Edinburgh Instruments). The work function of samples was tested by Scanning Kelvin Probe (SKP) (SKP5050 system, Scotland).

2.6. Photothermal Test

The photothermal test of as-prepared samples was carried out as follows. About 0.1 g of sample was laid out flat on white weighing paper (Figure S2) and the initial temperature was controlled at room temperature. The temperature of the sample was

measured using the Testo 865 infrared thermography. In the water temperature evolution test, 0.05 g photocatalyst was dispersed in 30 mL of water and kept magnetically stirred, and the corresponding temperature was recorded every 10 min by infrared thermal imager Testo 865. A 300 W xenon lamp (CEL-HXF300, Beijing China Education Au-light Co., Ltd., Beijing, China) was used as the light source for all the photothermal experiments, with a distance of approximately 20 cm between the light source and the sample.

2.7. Photocatalytic Performance Assessment

The photocatalytic pollutant degradation reactions were carried out on a multi-purpose photochemical reaction system (CEL-LAB500E4, Beijing China Education Au-light Co., Ltd.). About 50 mg of the photocatalyst was added to 100 mL of a solution containing TC (10 mg/L). Before the photocatalytic experiments, the solution containing the pollutant and the photocatalyst was placed in a dark room for 30 min to get the adsorption-desorption equilibrium. Then, the solution was irradiated under a 300 W xenon lamp with circulating water jacket (CEL-HXF300, Beijing China Education Au-light Co., Ltd.). Every 20 min, 3 mL of each liquid sample was removed from the beaker and filtered with 0.22 μm Millipore filter heads. Concentrations were subsequently tested using a high-performance liquid chromatograph (LC-3100).

The photocatalytic hydrogen evolution reaction was performed on the all-glass automatic online trace gas analysis system (Labsolar-6A, Beijing Perfect light Technology Co., Ltd., Beijing, China). With Labsolar-6A, a 300 W Xenon lamp (Microsolar300, Beijing Perfect light Technology Co., Ltd.) was used as the simulated sunlight spectral source. The as-prepared catalyst (10 mg) was uniformly dispersed by using a magnetic stirrer in 120 mL of methanol solution (containing H_2O/methanol, v/v = 90:30). The temperature of the reaction was kept at 298 K by cool flowing water. During the irradiation process, a hydrogen sample (0.5 mL) was extracted from the reactor at a given interval and the amount of hydrogen produced was analyzed by an online gas chromatograph (GC-7900).

3. Results and Discussion

3.1. Physical Phase Composition and Energy Band Structure

The crystal structures of g-C_3N_4 nanosheets, hexagonal α-Fe_2O_3 nanosheets, α-Fe_2O_3/g-C_3N_4 2D/2D heterojunction and Ag/α-Fe_2O_3/g-C_3N_4 ternary heterojunction were analyzed by XRD pattern, as shown in Figure 2a. The g-C_3N_4 has two distinct peaks at 12.8° and 27.7°, which were derived from the repeating unit and interlayer stacking within the carbon nitride plane, corresponding to two crystal planes (100) and (002), respectively [48]. The characteristic peaks of α-Fe_2O_3 at 24.1, 33.2, 35.7, 40.8, 49.5, 54.1, 62.5, and 64.1° correspond to the crystal faces of (012), (104), (110), (113), (024), (116), (214), and (300) on standard α-Fe_2O_3 cards (JCPDS No. 33-0664), respectively. The sharp XRD peaks indicate the high crystallinity of α-Fe_2O_3. The characteristic peaks of g-C_3N_4 and α-Fe_2O_3 are observed in the α-Fe_2O_3/g-C_3N_4 composite sample, indicating that the α-Fe_2O_3/g-C_3N_4 heterojunction photocatalyst was successfully prepared. The diffraction peaks of Ag were not observed in the XRD patterns of the Ag/α-Fe_2O_3/g-C_3N_4 ternary composites due to the low loading of Ag nanoparticles [40,43,47]. However, in the XPS with higher sensitivity, all the characteristic peaks of the α-Fe_2O_3 and g-C_3N_4 appeared in the XPS survey spectrum of Ag/α-Fe_2O_3/g-C_3N_4 composites, and the characteristic peaks of Ag were observed near 367 and 373 eV, indicating that the Ag/α-Fe_2O_3/g-C_3N_4 ternary composites were successfully prepared (Figure 2b) [47,49]. The light absorption properties of each prepared catalytic material were characterized by UV-vis diffuse reflectance spectroscopy (UV-vis DRS), Figure 2c shows that the optical response interval of the α-Fe_2O_3/g-C_3N_4 expands from 483 nm to 647 nm. The optical response of the Ag/α-Fe_2O_3/g-C_3N_4 ternary composite interval was further extended to the NIR region due to the LSPR of Ag nanoparticles. The intrinsic band gaps of g-C_3N_4 and α-Fe_2O_3 were estimated from the Tauc plots in Figure 2d, and the forbidden bandwidths of 2.04 and 2.58 eV for g-C_3N_4 and α-Fe_2O_3 were calculated from the intercepts of extrapolated lines in the *X*-axis, respectively. The energy band struc-

ture of Ag/α-Fe$_2$O$_3$/g-C$_3$N$_4$ was determined by VB-XPS. The test results of the VB-XPS in Figure 2e show that the VB positions of α-Fe$_2$O$_3$ and g-C$_3$N$_4$ are 2.36 and 1.35 eV relative to the normal hydrogen electrode, respectively. The relative energy band positions of α-Fe$_2$O$_3$ and g-C$_3$N$_4$ can be calculated based on the relationship between the semiconductor VB and CB, as shown in Figure 2f, the energy band arrangement of α-Fe$_2$O$_3$ and g-C$_3$N$_4$ is similar to Type II heterojunction [50]. The g-C$_3$N$_4$ possesses a higher conduction band position and is more electronically reductive, and the α-Fe$_2$O$_3$ has a lower valence band position and strong hole oxidation, which means that α-Fe$_2$O$_3$ and g-C$_3$N$_4$ will form S-Scheme heterojunctions with both strong proton reduction and strong hole oxidation ability.
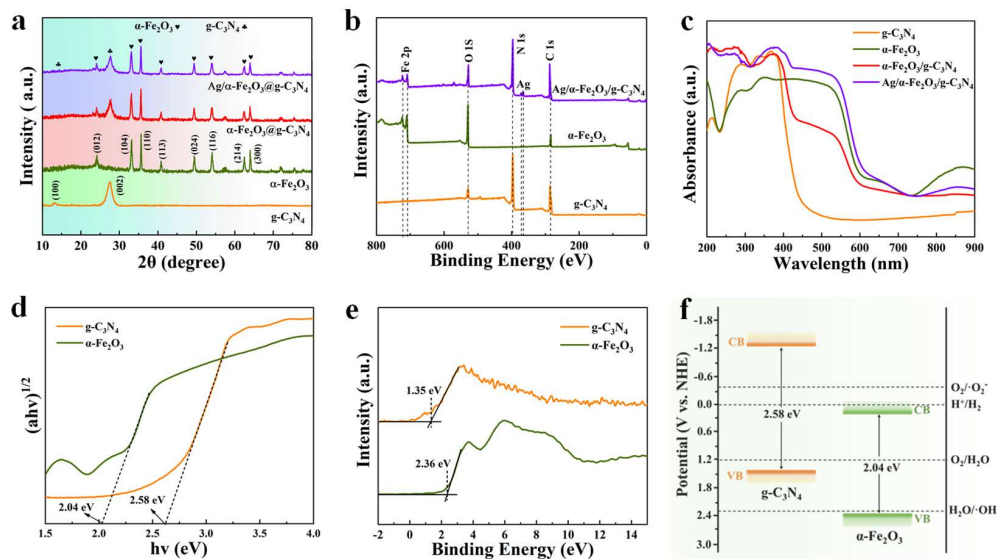
Figure 2. XRD patterns (**a**), XPS full spectra (**b**) and UV-vis DRS spectra (**c**) of g-C$_3$N$_4$, α-Fe$_2$O$_3$ and Ag/α-Fe$_2$O$_3$/g-C$_3$N$_4$, band gap (**d**), VB-XPS I (**e**) and relative energy band position maps (**f**) of g-C$_3$N$_4$ and α-Fe$_2$O$_3$.

3.2. Morphological and Structural Analysis

The morphological and structural characteristics of different photocatalysts were analyzed by TEM and SEM. In Figure 3a, g-C$_3$N$_4$ exhibits a self-supporting nanosheet morphology with a thickness of about 10 nm, which is further observed by the nearly transparent TEM image (Figure 3d). As shown in Figure 3b,g, the SEM and TEM images of α-Fe$_2$O$_3$ indicate that it is a hexagonal nanosheet with a size of about 220 nm and a thickness of about 20 nm. The SEM and TEM of α-Fe$_2$O$_3$/g-C$_3$N$_4$ composites are shown in Figure 3c,e, respectively, where two differently charged sheets of α-Fe$_2$O$_3$, g-C$_3$N$_4$ are closely adhered by electrostatic force. The hexagonal α-Fe$_2$O$_3$ nanosheets tightly adhere to the substrate composed of g-C$_3$N$_4$ with large size. This 2D/2D heterojunction shortens the distance that charge carriers have to migrate to the surface and facilitates the rapid involvement of carriers in chemical reactions [7]. Figure 3f clearly shows that Ag nanoparticles are dispersed on the α-Fe$_2$O$_3$/g-C$_3$N$_4$ surface. Figure 3h,i is high-resolution TEM images of the circled region, respectively, which show that the fully exposed active crystal plane of α-Fe$_2$O$_3$ is the (110) plane, while the 0.24 nm lattice spacing corresponds to the (111) crystal plane of Ag [51,52]. Figure 3j–n shows the energy dispersive X-ray spectroscopy (EDX) of Ag/α-Fe$_2$O$_3$/g-C$_3$N$_4$, which shows the presence of N (green), C (yellow), O (red), Fe (violet), and Ag (indigo) elements, further demonstrating the successful synthesis of Ag/α-Fe$_2$O$_3$/g-C$_3$N$_4$ ternary composite photocatalyst.
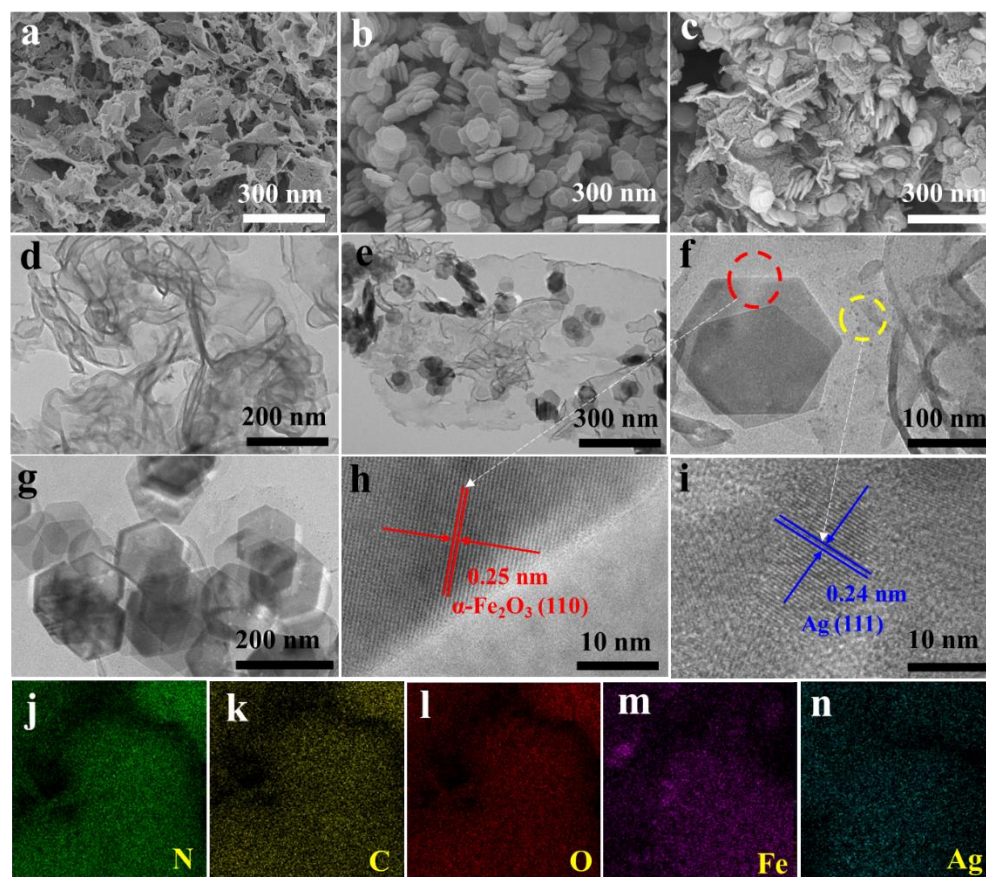
Figure 3. SEM image of (**a**) g-C$_3$N$_4$, (**b**) α-Fe$_2$O$_3$ and (**c**) α-Fe$_2$O$_3$/g-C$_3$N$_4$, TEM image of (**d**) g-C$_3$N$_4$, (**e**) α-Fe$_2$O$_3$/g-C$_3$N$_4$, (**f**) Ag/α-Fe$_2$O$_3$/g-C$_3$N$_4$, (**g**) α-Fe$_2$O$_3$, HRTEM image of (**h**) α-Fe$_2$O$_3$ and (**i**) Ag nanoparticles, (**j**–**n**) SEM-EDX mapping of Ag/α-Fe$_2$O$_3$/g-C$_3$N$_4$.

3.3. Analysis of Charge Transfer Mechanism

The charge transfer upon contact in compound semiconductors is generally related to the work function of the materials. To study the charge movement between g-C$_3$N$_4$ and α-Fe$_2$O$_3$, the work functions of them were analyzed by SKP (Figure 4a). The test results are presented as relative values of Au, and the work function of the standard Au sample was 5.1 eV. The work functions of α-Fe$_2$O$_3$ and g-C$_3$N$_4$ were derived to be 5.61 and 4.54 eV from the difference between the test results and the work function of the standard Au sample. Apparently, g-C$_3$N$_4$ has a higher Fermi energy position relative to α-Fe$_2$O$_3$, and when they are in close contact to form a heterojunction, the difference in work function leads to the spontaneous diffusion of electrons from g-C$_3$N$_4$ to α-Fe$_2$O$_3$ and form electron depletion and electron aggregation layers at the contact interface, which is the reason for the formation of the internal electric field. In addition, changes in element valence and electron density lead to chemical shifts in XPS, so the charge transfer mechanism of α-Fe$_2$O$_3$/g-C$_3$N$_4$ heterojunction can be analyzed by in situ irradiated XPS. Peaks in the Ag 3d XPS spectrum appear at 373.3 and 367.3 eV, originating from Ag 3d$_{5/2}$ and Ag 3d$_{3/2}$ with a difference of 6.0 eV between the two peaks, indicating that Ag exists as a monomeric form (Figure 4b) [49]. Figure 4c shows that the peaks of C1s located at 286.5 and 288.3 eV are attributed to C-N and C-N=C in g-C$_3$N$_4$, and the carbon peak at 284.8 eV is used to calibrate the other peaks. The peaks of N1s at 398.5, 399.8, and 400.8 eV in Figure 4d are assigned to C-N=C, C-(N)$_3$ and C-N-H in g-C$_3$N$_4$ [53]. Upon contact between α-Fe$_2$O$_3$ and g-C$_3$N$_4$, electrons transfer from g-C$_3$N$_4$ to α-Fe$_2$O$_3$ due to the difference in work functions. Both the peaks of C and N move toward higher binding energies after losing electrons. The electrons in the CB of α-Fe$_2$O$_3$ move to g-C$_3$N$_4$ driven by the internal electric field under light, and the peaks of N and C move toward lower binding energy after

g-C_3N_4 gaining electrons. The peaks of Fe 2p appeared at 711.2, 719.0, and 724.3 eV in Figure 4e, corresponding to Fe $2p_{3/2}$, Fe^{3+}, and Fe $2p_{1/2}$, respectively. Figure 4f shows that the characteristic peaks of O1s are located at 529.7 and 531.4 eV, attributing to lattice oxygen and adsorbed oxygen in α-Fe_2O_3, respectively, and the peak at 532.8 eV is from water adsorbed by the composite photocatalyst [54,55]. The shifting trend of O and Fe in α-Fe_2O_3/g-C_3N_4 before and after light illuminating is opposite to that of g-C_3N_4. α-Fe_2O_3 gets electrons when a heterojunction is formed, and its binding energy decreased. However, after illumination, α-Fe_2O_3 loses electrons and its binding energy rises [13,14,19]. Kelvin probe and in situ irradiated XPS results demonstrate the charge transfer mode of α-Fe_2O_3/g-C_3N_4 S-Scheme heterojunction, as shown in Figure 4g. Electrons move from g-C_3N_4 to α-Fe_2O_3 due to the difference of work function between α-Fe_2O_3 and g-C_3N_4, and an internal electric field is formed at the interface of the heterojunction, and the energy band bending of α-Fe_2O_3 and g-C_3N_4 caused by the electrostatic repulsion. When the α-Fe_2O_3/g-C_3N_4 heterojunction photocatalyst is excited by light, the electrons in the CB of α-Fe_2O_3 move to the VB of g-C_3N_4 and compound with the holes under the effect of internal electric field and energy band bending, so that the α-Fe_2O_3/g-C_3N_4 heterojunction maintains strong redox properties.

3.4. Photothermal Effect Evaluation

The photothermal effect of the catalyst was characterized by infrared thermography. Figure 5a,b shows the change of surface temperature of the pure g-C_3N_4 and ternary heterojunction photocatalysts with the increased light time in the air, respectively. The initial temperature of the g-C_3N_4 powder surface was 26.6 °C, and then increased quickly to 54.9 °C after 90 s of light illumination, while the temperature of Ag/α-Fe_2O_3/g-C_3N_4 powder increased from 26.5 °C to 173 °C at the same condition, which was 5.57 times higher than that of the original g-C_3N_4, indicating that the construction of heterojunction and the modification of Ag nanoparticles significantly improved the photothermal conversion ability of the ternary composite. The photothermal performance of the powder catalysts in real reactions was investigated by photothermal experiments in water. Figure 5c,d shows the temperature changes of pristine g-C_3N_4 and the ternary composite sample with the increase of light time in the water, respectively. The temperature of g-C_3N_4 solution system under light increased from the initial 19.4 °C to 32.3 °C with a temperature increase of 12.9 °C, while the temperature of the ternary heterojunction increased from the initial 19.7 °C to 59.1 °C at the same condition, which was three times higher than that of pure g-C_3N_4, indicating that Ag/α-Fe_2O_3/g-C_3N_4 offers a more significant photothermal effect. Ag/α-Fe_2O_3/g-C_3N_4 ternary photocatalysts can convert part of the absorbed photon energy into thermal energy through the photothermal effect to form a local thermal environment near the catalyst surface in a photocatalytic process, thus increasing the near-field chemical reaction rate of the catalyst and enhancing the photocatalytic performance of the catalyst [13,56,57].
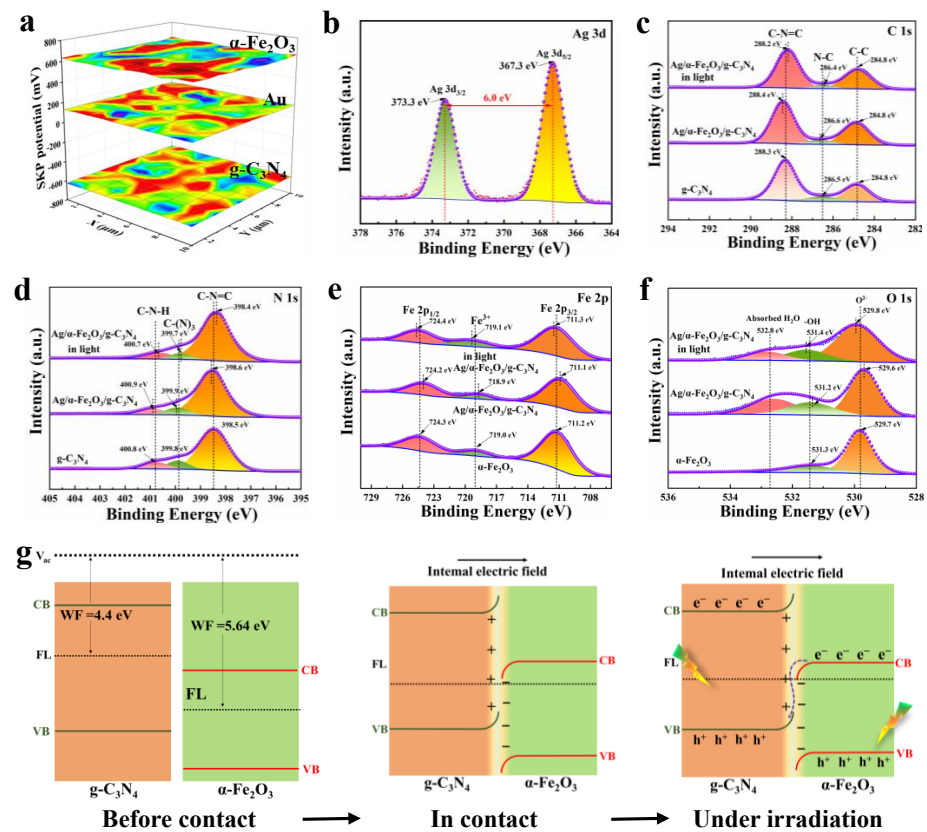
Figure 4. Work function of α-Fe$_2$O$_3$ and g-C$_3$N$_4$ (**a**). Ag 3d XPS spectra (**b**), the XPS spectra of C 1s (**c**) and N 1s (**d**) of g-C$_3$N$_4$ and Ag/α-Fe$_2$O$_3$/g-C$_3$N$_4$, the XPS spectra of O 1s (**e**) and Fe 2p (**f**) of α-Fe$_2$O$_3$ and Ag/α-Fe$_2$O$_3$/g-C$_3$N$_4$. (**g**) The formation mechanism of S-Scheme heterojunctions.
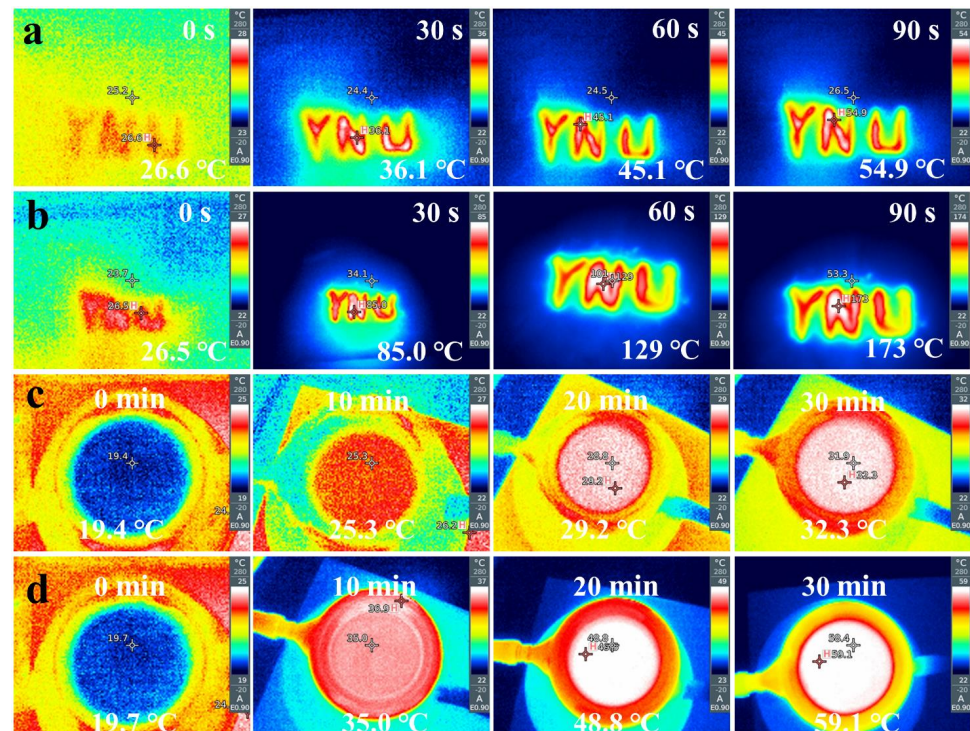
Figure 5. Temperature-light time trends of g-C$_3$N$_4$ (**a**), Ag/α-Fe$_2$O$_3$/g-C$_3$N$_4$ (**b**) in the air. Temperature-light time trends of g-C$_3$N$_4$ (**c**), Ag/α-Fe$_2$O$_3$/g-C$_3$N$_4$ (**d**) in the water.

3.5. Photocatalytic Hydrogen Production and Pollutant Degradation Testing

Photocatalytic hydrogen production and degradation of TC experiments were performed to evaluate the activity of prepared catalysts. The synthesis process was optimized by degrading TC experiment. The photocatalytic performance of α-Fe_2O_3/g-C_3N_4 heterojunction was affected by the ratio of α-Fe_2O_3. The best degradation effect of TC was obtained when the weight ratio of α-Fe_2O_3 was 30wt%. The α-Fe_2O_3/g-C_3N_4 will produce serious agglomeration if α-Fe_2O_3 is too much (Figure S3), and the performance improvement is not obvious if α-Fe_2O_3 is too low (Figure S4). When the loading amount of Ag nanoparticles is 0.5wt%, Ag/α-Fe_2O_3/g-C_3N_4 has the best photocatalytic performance (Figure S5). The performance of the catalyst is not improved as the silver nitrate increased, indicating that the content of Ag particles loaded on α-Fe_2O_3/g-C_3N_4 by photoreduction process was relatively low, which is beneficial to improve the dispersion of Ag nanoparticles. Therefore, samples with optimal composite ratios were used to assess the contribution of constructing heterojunctions and plasma Ag modifications. Figure 6a shows that the original g-C_3N_4 photocatalytic hydrogen production rate was 387.45 μmol g^{-1} h^{-1}, and the hydrogen production rate of ternary heterojunction reached 3125.62 μmol g^{-1} h^{-1}. After constructing the S-Scheme heterojunction and completing the surface-engineered plasma Ag modification, the hydrogen production rate reached more than eight times of the original one, and there was no significant decay during the 1200 min cycle (Figure 6b). Ag/α-Fe_2O_3/g-C_3N_4 has a high hydrogen production efficiency compared to other recently reported photocatalysts of the same type (Table S1). Ag nanoparticles not only improve carrier separation through LSPR but also provide additional active sites for hydrogen production [33,34]. In addition, Ag/α-Fe_2O_3/g-C_3N_4 also showed the best performance in the degradation experiments of TC with a 93.6% degradation rate in 150 min (Figure 6c), and approximately maintained this degradation rate for all five cycles (Figure 6d). The first-order reaction kinetic curves show that apparent reaction rate of Ag/α-Fe_2O_3/g-C_3N_4 was 2.6 times that of pure g-C_3N_4 (Figure 6e), and Ag/α-Fe_2O_3/g-C_3N_4 has relatively excellent TC degradation compared to other recently reported photocatalysts of the same type (Table S2), which was the combined effect of S-Scheme heterojunction and photothermal effect to enhance the chemical reaction rate [19,56]. The radical quenching experiments showed that $\cdot$OH played a dominant role in the degradation of TC, followed by vacancies, and the superoxide radical ($\cdot O_2^{-2}$) at last (Figure 6f) [58]. The mineralization rate of ternary heterojunction for TC reached 49.26%, which was 44.3 times that of pristine g-C_3N_4, indicating that the redox ability of the composite sample was substantially enhanced (Figure 6g). To investigate the promotion of photocatalytic degradation reaction by photothermal effect, we conducted a circulating cooling experiment. The effect of temperature on the degradation of TC by Ag/α-Fe_2O_3/g-C_3N_4 was relatively obvious from Figure 6h, and the degradation efficiency decreased significantly when the circulating cooling water was turned on. The reaction rate in the Ag/α-Fe_2O_3/g-C_3N_4 degradation of TC without cooling water was 1.5 times higher than that with cooling water (Figure 6i), which indicated that the heat generated by the photothermal effect could effectively promote the photocatalytic catalytic reaction rate.
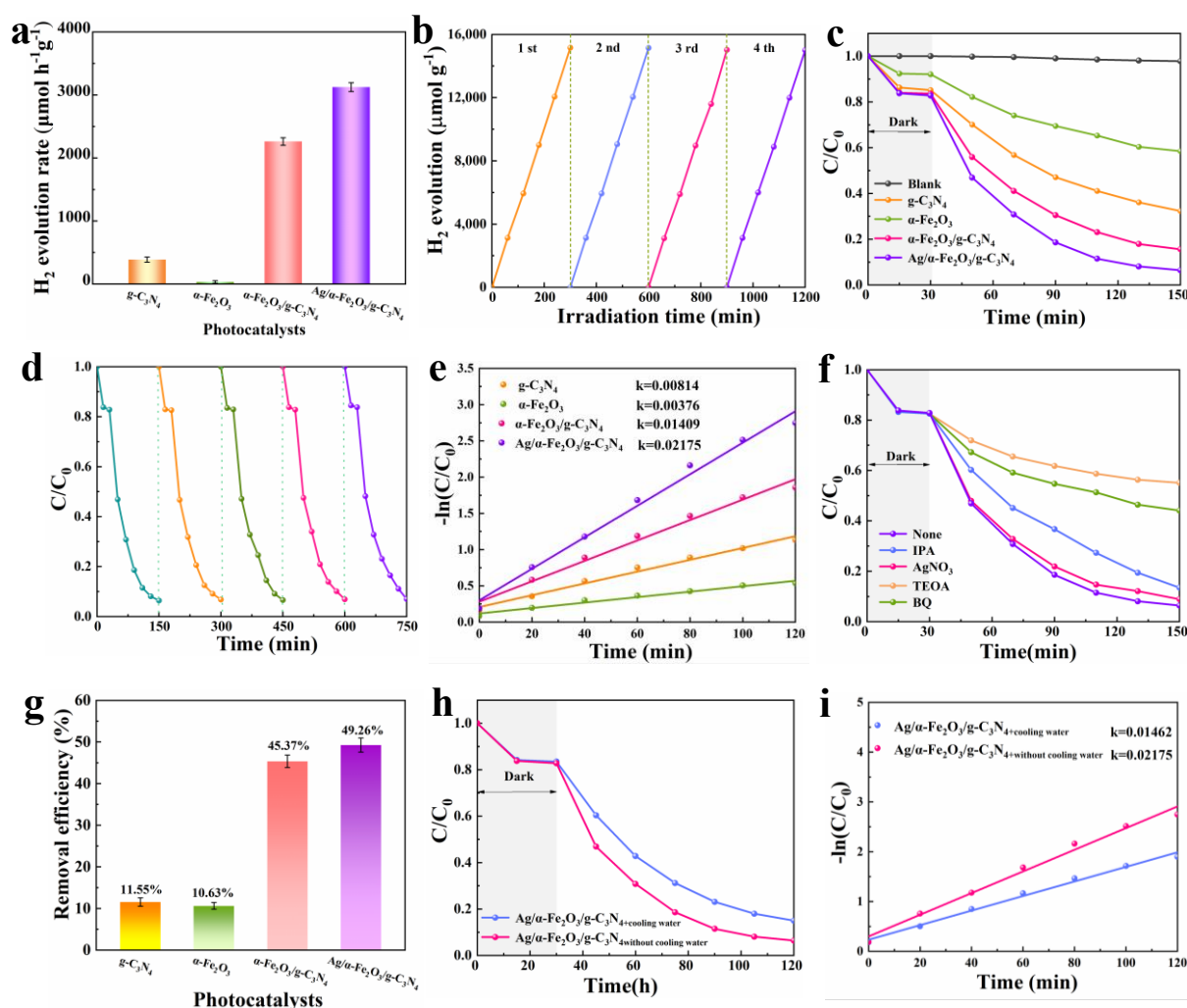
Figure 6. Hydrogen production rate (**a**), hydrogen production rate cycling performance (**b**), photocatalytic-Fenton degradation performance (**c**), degradation cycling performance (**d**), the first-order kinetic curves (**e**), free radical quenching experiments (**f**), contaminant mineralization performance (**g**), cyclic cooling experiments (**h**), cyclic cooling first-order kinetic curves (**i**) for g-C_3N_4, α-Fe_2O_3, α-Fe_2O_3/g-C_3N_4 and Ag/α-Fe_2O_3/g-C_3N_4.

3.6. Photoelectrochemical Performance Analysis

To investigate the charge transport kinetics of the photocatalyst, a series of photoelectrochemical tests was performed. Figure 7a shows that Ag/α-Fe_2O_3/g-C_3N_4 has the best transient photocurrent response, indicating its high concentration of photogenerated carriers. The low impedance implies a low carrier migration resistance in Ag/α-Fe_2O_3/g-C_3N_4, which facilitates charge separation (Figure 7b). The steady-state PL shows the lowest luminescence intensity in Ag/α-Fe_2O_3/g-C_3N_4, demonstrating that the S-Scheme heterojunction effectively suppresses the radiative relaxation in Ag/α-Fe_2O_3/g-C_3N_4 (Figure 7c). Time-resolved photoluminescence spectroscopy (TRPL) can accurately analyze the carrier lifetime in the catalysts, and the fitted results in Figure 7d show that the fluorescence lifetime of Ag/α-Fe_2O_3/g-C_3N_4 is 4.57 ns, which is 3.7 times that of the pristine g-C_3N_4, indicating that the S-Scheme heterojunction and surface plasmon resonance effects enhance the separation and transport of carriers. The electron paramagnetic resonance (EPR) experiments reveal the mechanism of the interaction between carriers and surface-adsorbed molecules in the catalysts. The $\cdot O_2^-$ and $\cdot OH$ production under light for each catalyst is shown in Figure 7e,f, respectively. The results of DMPO-$\cdot O$ showed that α-Fe_2O_3 could not generate $\cdot O_2^-$ under light, which is due to its conduction band electron reduction abil-

ity is not sufficient to reduce O_2 to generate $\cdot O_2^-$. The signal of $\cdot O_2^-$ was detected after α-Fe_2O_3 was compounded with g-C_3N_4, and the Ag nanoparticle modification further enhanced the $\cdot O_2^-$ signal. The DMPO-$\cdot$OH results showed that no $\cdot$OH signal is detected in pure g-C_3N_4 due to insufficient oxidation capacity of the hole. α-Fe_2O_3/g-C_3N_4 and Ag/α-Fe_2O_3/g-C_3N_4 showed obvious $\cdot$OH characteristic signals, which indicated that the composite photocatalytic system can generate a large number of strongly oxidizing hydroxyl radicals under light to participate in the degradation reaction. This is consistent with the results of the free radical quenching experiments. The ERP test results further reveal that charge transfer similar to that of Type II heterojunctions does not occur in the composite photocatalytic system and that electrons and holes with strong redox capabilities are retained in the system. The mode of charge transfer in ternary heterojunctions is consistent with the S-Scheme mechanism [13,14].
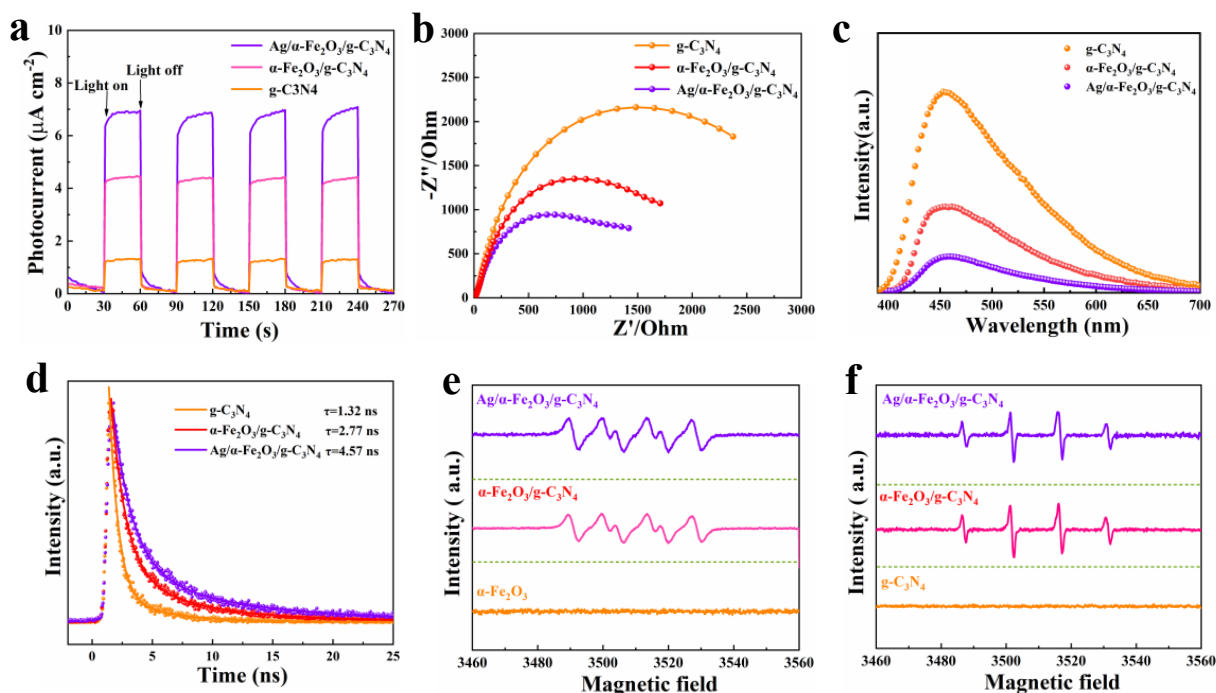

Figure 7. Photocurrent curves (**a**), impedance experiments (**b**), PL spectra (**c**), TRPL spectra (**d**), DMPO-$\cdot O_2^-$ signals under light (**e**), DMPO-$\cdot$OH signals under light (**f**) of g-C_3N_4, α-Fe_2O_3/g-C_3N_4 and Ag/α-Fe_2O_3/g-C_3N_4.

3.7. Mechanistic Analysis

　　Based on the above experimental phenomena and characterization results, we propose a photocatalytic mechanism for Ag/α-Fe_2O_3/g-C_3N_4 heterojunction. S-Scheme heterojunction, photothermal and photocatalytic-Fenton synergy for Ag/α-Fe_2O_3/g-C_3N_4 performance enhancement (Figure 8). The carrier generated by photoexcitation migrates directionally under the action of internal electric field and interfacial energy band bending, and its migration path follows the S-Scheme mechanism that electrons and holes stored in the VB of α-Fe_2O_3 and in the CB of g-C_3N_4, respectively. The electron with strong reducibility in g-C_3N_4 can capture free hydrogen and dissolved oxygen and generate H_2O_2 rapidly. The free electrons in the photocatalytic system can reduce part of Fe^{3+} to Fe^{2+} in α-Fe_2O_3, Fe^{2+} then react with H_2O_2 to produce a large amount of $\cdot$OH through the chain Fenton reaction. Moreover, a large number of high-energy electrons generated by the LSPR effect of Ag nanoparticles are injected into the S-Scheme heterojunction photocatalytic system, which facilitates the generation of strong oxidizing $\cdot$OH and $\cdot O_2^-$ and increases the concentration of free radicals in the system, and the heat generated will promote the rate

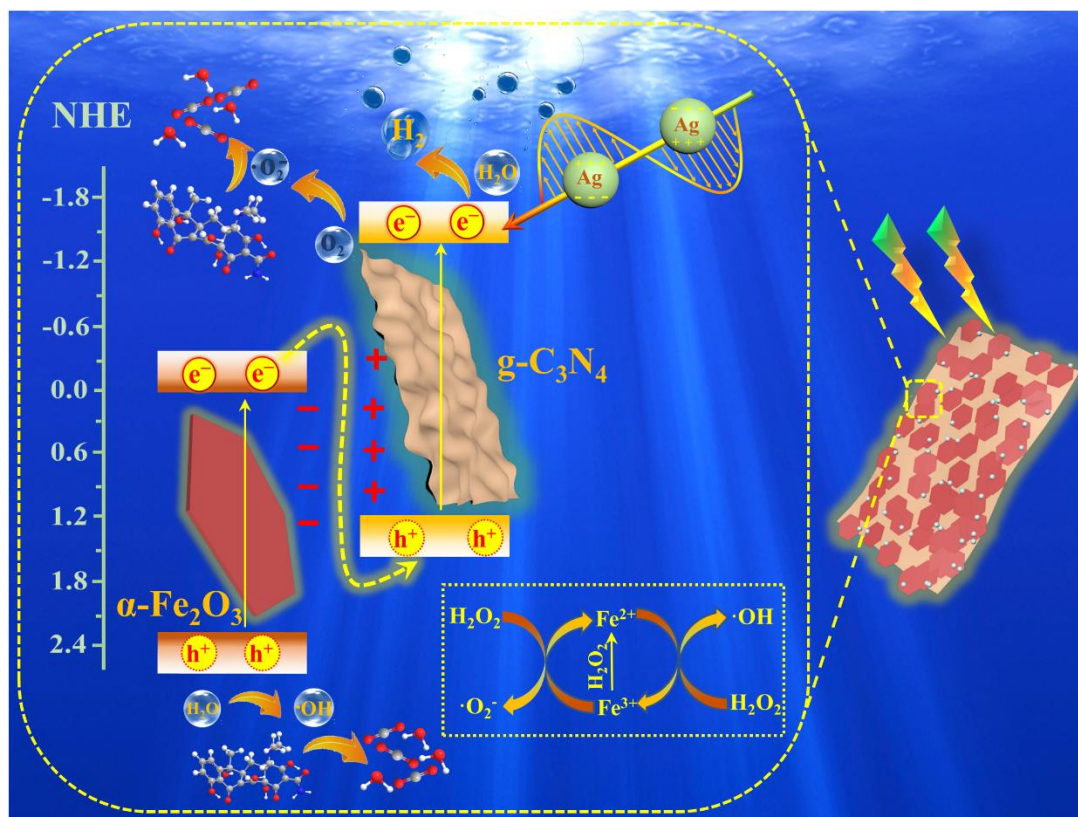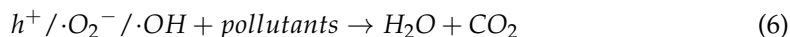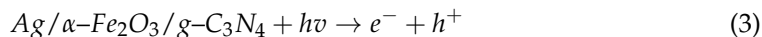of chemical reactions on the surface. This photocatalytic reaction process consists of the following steps:

$$Ag/\alpha\text{–}Fe_2O_3/g\text{–}C_3N_4 + hv \rightarrow e^- + h^+ \tag{3}$$

$$e^- + O_2 \rightarrow \cdot O_2^- \tag{4}$$

$$\cdot O_2^- + H^+ \rightarrow H_2O_2 \tag{5}$$

$$h^+/\cdot O_2^-/\cdot OH + pollutants \rightarrow H_2O + CO_2 \tag{6}$$

Figure 8. Schematic diagram of photocatalytic mechanism of Ag/α-Fe₂O₃/g-C₃N₄ S-Scheme heterojunction.

The photocatalytic-Fenton coupling system increases the number of active radicals effectively, and the internal energy generated by the photothermal effect can be activated to promote the dissociation of water molecules and accelerate the chemical reaction kinetics. The synergistic effect of S-Scheme heterojunctions, photothermal and photocatalytic-Fenton enabled the Ag/α-Fe₂O₃/g-C₃N₄ ternary heterojunction to exhibit satisfactory photocatalytic performance [23–25].

4. Conclusions

In conclusion, we have successfully prepared plasma Ag-modified α-Fe₂O₃/g-C₃N₄ S-Scheme heterojunctions by electrostatic self-assembly and light deposition strategy. The photocatalytic hydrogen production rate of Ag/α-Fe₂O₃/g-C₃N₄ reached 3125 μmol g⁻¹ h⁻¹, eight times that of pristine g-C₃N₄, and the photocatalytic TC degradation rate was as high as 93.6% within 120 min. The reason for this enhanced performance may arise from the following: (1)The S-Scheme heterojunction composed of 2D/2D nanosheets facilitates the spatial separation of charge carriers and the full exposure of active sites; (2) the photocatalytic-Fenton reaction helps to improve the carrier conversion and to enrich the number of active radicals in the reaction system; (3) the LSPR effect of Ag nanoparticles provides high-energy electrons the system to promote the separation of

carriers, and generates the photothermal effect to facilitate surface reaction kinetic. This synergistic catalytic strategy provides valuable insights for the construction of highly active photocatalytic systems.

Conflicts of Interest: The authors declare no conflict of interest.

References

1. Nishiyama, H.; Yamada, T.; Nakabayashi, M.; Maehara, Y.; Yamaguchi, M.; Kuromiya, Y.; Nagatsuma, Y.; Tokudome, H.; Akiyama, S.; Watanabe, T.; et al. Photocatalytic solar hydrogen production from water on a 100-m^2 scale. *Nature* **2021**, *598*, 304–307. [CrossRef]
2. Kosco, J.; Gonzalez, S.; Howells, C.T.; Fei, T.; Dong, Y.; Sougrat, R.; Harrison, G.T.; Firdaus, Y.; Sheelamanthula, R.; Purushothaman, B.; et al. Generation of long-lived charges in organic semiconductor heterojunction nanoparticles for efficient photocatalytic hydrogen evolution. *Nat. Energy* **2022**, *7*, 340–351. [CrossRef]
3. Song, L.; Wang, W.; Yue, J.P.; Jiang, Y.X.; Wei, M.K.; Zhang, H.P.; Yan, S.S.; Liao, L.L.; Yu, D.G. Visible-light photocatalytic di- and hydro-carboxylation of unactivated alkenes with CO$_2$. *Nat. Catal.* **2022**, *5*, 823–838. [CrossRef]
4. Zhang, X.; Ma, P.J.; Wang, C.; Gan, L.Y.; Chen, X.J.; Zhang, P.; Wang, Y.; Li, H.; Wang, L.H.; Zhou, X.Y.; et al. Unraveling the dual defect sites in graphite carbon nitride for ultra-high photocatalytic H$_2$O$_2$ evolution. *Energy Environ. Sci.* **2022**, *15*, 830–842. [CrossRef]
5. Wang, Y.; Qu, Y.; Qu, B.; Bai, L.; Liu, Y.; Yang, Z.-D.; Zhang, W.; Jing, L.; Fu, H. Construction of six-oxygen-coordinated single Ni sites on g-C$_3$N$_4$ with boron-oxo species for photocatalytic water-activation-induced CO$_2$ reduction. *Adv. Mater.* **2021**, *33*, 2105482. [CrossRef]
6. Wu, B.; Zhang, L.; Jiang, B.; Li, Q.; Tian, C.; Xie, Y.; Li, W.; Fu, H. Ultrathin porous carbon nitride bundles with an adjustable energy band structure toward simultaneous solar photocatalytic water splitting and selective phenylcarbinol oxidation. *Angew. Chem. Int. Ed.* **2021**, *60*, 4951. [CrossRef]
7. Wang, Y.; Liu, L.; Ma, T.; Zhang, Y.; Huang, H. 2D graphitic carbon nitride for energy conversion and storage. *Adv. Funct. Mater.* **2021**, *31*, 2102540. [CrossRef]
8. Che, H.; Gao, X.; Chen, J.; Hou, J.; Ao, Y.; Wang, P. Iodide-induced fragmentation of polymerized hydrophilic carbon nitride for high-performance quasi-homogeneous photocatalytic H$_2$O$_2$ production. *Angew. Chem. Int. Ed.* **2021**, *60*, 25546–25550. [CrossRef]
9. Hu, C.; Chen, F.; Wang, Y.; Tian, N.; Ma, T.; Zhang, Y.; Huang, H. Exceptional cocatalyst-free photo-enhanced piezocatalytic hydrogen evolution of carbon nitride nanosheets from strong in-plane polarization. *Adv. Mater.* **2021**, *33*, 2101751. [CrossRef]
10. Zhou, H.; Wang, M.; Wang, F. Oxygen-controlled photo-reforming of biopolyols to CO over Z-scheme CdS@g-C$_3$N$_4$. *Chem* **2022**, *8*, 465–479. [CrossRef]

11. Zhao, D.; Wang, Y.; Dong, C.L.; Huang, Y.C.; Chen, J.; Xue, F.; Shen, S.; Guo, L. Boron-doped nitrogen-deficient carbon nitride-based Z-scheme heterostructures for photocatalytic overall water splitting. *Nat. Energy* **2021**, *6*, 388–397. [CrossRef]

12. Tan, Y.; Chen, W.; Liao, G.; Li, X.; Wang, J.; Tang, Y.; Li, L. Strategy for improving photocatalytic ozonation activity of g-C_3N_4 by halogen doping for water purification. *Appl. Catal. B Environ.* **2022**, *306*, 121133. [CrossRef]

13. Zhang, L.; Zhang, J.; Yu, H.; Yu, J. Emerging S-scheme photocatalyst. *Adv. Mater.* **2022**, *34*, 2107668. [CrossRef] [PubMed]

14. Xu, Q.; Zhang, L.; Cheng, B.; Fan, J.; Yu, J. S-scheme heterojunction photocatalyst. *Chem* **2020**, *6*, 1543–1559. [CrossRef]

15. Wang, J.; Yu, Y.; Cui, J.; Li, X.; Zhang, Y.; Wang, C.; Yu, X.; Ye, J. Defective g-C_3N_4/covalent organic framework van der Waals heterojunction toward highly efficient S-scheme CO_2 photoreduction. *Appl. Catal. B Environ.* **2022**, *301*, 120814. [CrossRef]

16. Ren, Y.; Han, Q.; Zhao, Y.; Wen, H.; Jiang, Z. The exploration of metal-free catalyst g-C_3N_4 for NO degradation. *J. Hazard. Mater.* **2021**, *404*, 124153. [CrossRef]

17. Wang, J.; Wang, S. A critical review on graphitic carbon nitride (g-C_3N_4)-based materials: Preparation, modification and environmental application. *Coord. Chem. Rev.* **2022**, *453*, 214338. [CrossRef]

18. Yuan, X.; Qu, S.; Huang, X.; Xue, X.; Yuan, C.; Wang, S.; Wei, L.; Cai, P. Design of core-shelled g-C_3N_4@ZIF-8 photocatalyst with enhanced tetracycline adsorption for boosting photocatalytic degradation. *Chem. Eng. J.* **2021**, *416*, 129148. [CrossRef]

19. Gong, S.; Teng, X.; Niu, Y.; Liu, X.; Xu, M.; Xu, C; Ji, L.; Chen, Z. Construction of S-Scheme 0D/2D heterostructures for enhanced visible-light-driven CO_2 reduction. *Appl. Catal. B Environ.* **2021**, *298*, 120521. [CrossRef]

20. Moradi, S.; Isari, A.A.; Hayati, F.; Kalantary, R.R.; Kakavandi, B. Co-implanting of TiO_2 and liquid-phase-delaminated g-C_3N_4 on multi-functional graphene nanobridges for enhancing photocatalytic degradation of acetaminophen. *Chem. Eng. J.* **2021**, *414*, 128618. [CrossRef]

21. Yang, Y.; Chen, J.; Chen, Z.; Yu, Z.; Xue, J.; Luan, T.; Chen, S.; Zhou, S. Mechanisms of polystyrene microplastic degradation by the microbially driven Fenton reaction. *Water Res.* **2022**, *223*, 118979. [CrossRef] [PubMed]

22. Qi, Y.; Mei, Y.; Li, J.; Yao, T.; Yang, Y.; Jia, W.; Tong, X.; Wu, J.; Xin, B. Highly efficient microwave-assisted Fenton degradation of metacycline using pine-needle-like $CuCo_2O_4$ nanocatalyst. *Chem. Eng. J.* **2019**, *373*, 1158–1167. [CrossRef]

23. Sun, H.; Xie, G.; He, D.; Zhang, L. Ascorbic acid promoted magnetite Fenton degradation of alachlor: Mechanistic insights and kinetic modeling. *Appl. Catal. B Environ.* **2020**, *267*, 118383. [CrossRef]

24. Zhang, H.; Li, L.; Chen, N.; Ben, H.; Zhan, G.; Sun, H.; Li, Q.; Sun, J.; Zhang, L. Hydroxylamine enables rapid heterogeneous-homogeneous coupled Fenton sulfamethazine degradation on ferric phosphate. *Appl. Catal. B Environ.* **2022**, *312*, 121410. [CrossRef]

25. Hu, J.; Li, J.; Cui, J.; An, W.; Liu, L.; Liang, Y.; Cui, W. Surface oxygen vacancies enriched FeOOH/Bi_2MoO_6 photocatalysis-fenton synergy degradation of organic pollutants. *J. Hazard. Mater.* **2020**, *384*, 121399. [CrossRef]

26. Huang, S.; Zheng, B.F.; Tang, Z.Y.; Mai, X.Q.; Ouyang, T.; Liu, Z.Q. CH=OH selective oxidation to HCHO on Z-scheme Fe_2O_3/g-C_3N_4 hybrid: The rate-determining step of C-H bond scission. *Chem. Eng. J.* **2021**, *422*, 130086. [CrossRef]

27. Chen, W.; Yang, S.; Liu, H.; Huang, F.; Shao, Q.; Liu, L.; Sun, J.; Sun, C.; Chen, D.; Dong, L. Single-Atom Ce-Modified α-Fe_2O_3 for Selective Catalytic Reduction of NO with NH_3. *Environ. Sci. Technol.* **2022**, *56*, 10442–10453. [CrossRef]

28. Moradlou, O.; Rabiei, Z.; Banazadeh, A.; Warzywoda, J.; Zirak, M. Carbon quantum dots as nano-scaffolds for α-Fe=O_3 growth: Preparation of Ti/CQD@α-Fe_2O_3 photoanode for water splitting under visible light irradiation. *Appl. Catal. B Environ.* **2018**, *227*, 178–189. [CrossRef]

29. Yang, Q.; Du, J.; Li, J.; Wu, Y.; Zhou, Y.; Yang, Y.; Yang, D.; He, H. Thermodynamic and kinetic influence of oxygen vacancies on the solar water oxidation reaction of α-Fe_2O_3 photoanodes. *ACS Appl. Mater. Interfaces* **2020**, *12*, 11625–11634. [CrossRef]

30. He, B.C.; Zhang, C.; Luo, P.P.; Li, Y.; Lu, T.B. Integrating Z-scheme heterojunction of Co_1-C_3N_4@α-Fe_2O_3 for efficient visible-light-driven photocatalytic CO_2 reduction. *Green Chem.* **2020**, *22*, 7552–7559. [CrossRef]

31. Li, F.; Huang, T.; Sun, F.; Chen, L.; Li, P.; Shao, F.; Yang, X.; Liu, W. Ferric oxide nanoclusters with low-spin FeIII anchored g-C_3N_4 rod for boosting photocatalytic activity and degradation of diclofenac in water under solar light. *Appl. Catal. B Environ.* **2022**, *317*, 121725. [CrossRef]

32. Wang, R.; Che, G.; Wang, C.; Liu, C.; Liu, B.; Ohtani, B.; Liu, Y.; Zhang, X. Alcohol plasma processed surface amorphization for photocatalysis. *ACS Catal.* **2022**, *12*, 12206–12216. [CrossRef]

33. Verma, R.; Belgamwar, R.; Polshettiwar, V. Plasmonic photocatalysis for CO_2 conversion to chemicals and fuels. *ACS Mater. Lett.* **2021**, *3*, 574–598. [CrossRef]

34. An, X.; Kays, J.C.; Lightcap, I.V.; Ouyang, T.; Dennis, A.M.; Reinhard, B.M. Wavelength-dependent bifunctional plasmonic photocatalysis in Au/chalcopyrite hybrid nanostructures. *ACS Nano* **2022**, *16*, 6813–6824. [CrossRef]

35. Qiu, J.L.; Su, J.; Muhammad, N.; Zheng, W.T.; Yue, C.L.; Liu, F.Q.; Zuo, J.L.; Ding, Z.J. Facile encapsulating Ag nanoparticles into a tetrathiafulvalene-based Zr-MOF for enhanced photocatalysis. *Chem. Eng. J.* **2022**, *427*, 131970. [CrossRef]

36. Zhou, X.; Shen, B.; Zhai, J.; Hedin, N. Reactive oxygenated species generated on iodide-doped $BiVO_4$/$BaTiO_3$ heterostructures with Ag/Cu nanoparticles by coupled piezophototronic effect and plasmonic excitation. *Adv. Funct. Mater.* **2021**, *31*, 2009594. [CrossRef]

37. Zhao, W.; Ding, T.; Wang, Y.; Wu, M.; Jin, W.; Tian, Y.; Li, X. Decorating Ag/AgCl on UiO-66-NH_2: Synergy between Ag plasmons and heterostructure for the realization of efficient visible light photocatalysis. *Chin. J. Catal.* **2019**, *40*, 1187–1197. [CrossRef]

38. Lei, Y.; Xu, S.; Ding, M.; Li, L.; Sun, Q.; Wang, Z.L. Enhanced photocatalysis by synergistic piezotronic effect and exciton-plasmon interaction based on (Ag-Ag_2S)/$BaTiO_3$ heterostructures. *Adv. Funct. Mater.* **2020**, *30*, 2005716. [CrossRef]

39. Liu, M.; Jin, X.; Li, S.; Billeau, J.B.; Peng, T.; Li, H.; Zhao, L.; Zhang, Z.; Claverie, J.P.; Razzari, L.; et al. Enhancement of scattering and near field of TiO$_2$-Au nanohybrids using a silver resonator for efficient plasmonic photocatalysis. *ACS Appl. Mater. Interfaces* **2021**, *13*, 34714–34723. [CrossRef] [PubMed]

40. Kashyap, T.; Biswas, S.; Ahmed, S.; Kalita, D.; Nath, P.; Choudhury, B. Plasmon activation versus plasmon quenching on the overall photocatalytic performance of Ag/Au bimetal decorated g-C$_3$N$_4$ nanosheets under selective photoexcitation: A mechanistic understanding with experiment and theory. *Appl. Catal. B Environ.* **2021**, *298*, 120614. [CrossRef]

41. Lee, S.; Hwang, H.; Lee, W.; Schebarchov, D.; Wy, Y.; Grand, J.; Auguié, B.; Wi, D.H.; Cortés, E.; Han, S.W. Core-shell bimetallic nanoparticle trimers for efficient light-to-chemical energy conversion. *ACS Energy Lett.* **2020**, *5*, 3881–3890. [CrossRef]

42. Koya, A.N.; Zhu, X.; Ohannesian, N.; Yanik, A.A.; Alabastri, A.; Zaccaria, R.P; Krahne, R.; Shih, W.C.; Garoli, D. Nanoporous metals: From plasmonic properties to applications in enhanced spectroscopy and photocatalysis. *ACS Nano* **2021**, *15*, 6038–6060. [CrossRef]

43. Mo, J.; Barbosa, E.C.; Wu, S.; Li, Y.; Sun, Y.; Xiang, W.; Li, T.; Pu, S.; Robertson, A.; Wu, T.S.; et al. Atomic-precision tailoring of Au-Ag core-shell composite nanoparticles for direct electrochemical-plasmonic hydrogen evolution in water splitting. *Adv. Funct. Mater.* **2021**, *31*, 2102517. [CrossRef]

44. Dutta, A.; Schürmann, R.; Kogikoski, S., Jr.; Mueller, N.S.; Reich, S.; Bald, I. Kinetics and mechanism of plasmon-driven dehalogenation reaction of brominated purine nucleobases on Ag and Au. *ACS Catal.* **2021**, *11*, 8370–8381. [CrossRef]

45. Zhang, X.; Shi, R.; Li, Z.; Zhao, J.; Huang, H.; Zhou, C.; Zhang, T. Photothermal-assisted photocatalytic nitrogen oxidation to nitric acid on palladium-decorated titanium oxide. *Adv. Energy Mater.* **2022**, *12*, 2103740. [CrossRef]

46. Xiao, Y.; Wang, K.; Yang, Z.; Xing, Z.; Li, Z.; Pan, K.; Zhou, W. Plasma Cu-decorated TiO$_{2-x}$/CoP particle-level hierarchical heterojunctions with enhanced photocatalytic-photothermal performance. *J. Hazard. Mater.* **2021**, *414*, 125487. [CrossRef]

47. Guo, M.; Xing, Z.; Zhao, T.; Qiu, Y.; Tao, B.; Li, Z.; Zhou, W. Hollow flower-like polyhedral α-Fe$_2$O$_3$/Defective MoS$_2$/Ag Z-scheme heterojunctions with enhanced photocatalytic-Fenton performance via surface plasmon resonance and photothermal effects. *Appl. Catal. B Environ.* **2020**, *272*, 118978. [CrossRef]

48. Zhao, D.; Dong, C.L.; Wang, B.; Chen, C.; Huang, Y.C.; Diao, Z.; Li, S.; Guo, L.; Shen, S. Synergy of dopants and defects in graphitic carbon nitride with exceptionally modulated band structures for efficient photocatalytic oxygen evolution. *Adv. Mater.* **2019**, *31*, 1903545. [CrossRef] [PubMed]

49. Kong, W.; Xing, Z.; Fang, B.; Cui, Y.; Li, Z.; Zhou, W. Plasmon Ag/Na-doped defective graphite carbon nitride/NiFe layered double hydroxides Z-scheme heterojunctions toward optimized photothermal-photocatalytic-Fenton performance. *Appl. Catal. B Environ.* **2022**, *304*, 120969. [CrossRef]

50. Shin, J.; Eo, J.S.; Jeon, T.; Lee, T.; Wang, G. Advances of Various Heterogeneous Structure Types in Molecular Junction Systems and Their Charge Transport Properties. *Adv. Sci.* **2022**, *9*, 2202399. [CrossRef]

51. She, X.J.; Wu, J.J.; Xu, H.; Zhong, J.; Wang, Y.; Song, Y.; Nie, K.; Liu, Y.; Yang, Y.; Yang, C.; et al. High efficiency photocatalytic water splitting using 2D α-Fe$_2$O$_3$/g-C$_3$N$_4$ Z-scheme catalysts. *Adv. Energy Mater.* **2017**, *7*, 1700025. [CrossRef]

52. Mandal, S.; Nanavati, S.P.; Willock, D.J.; Ananthakrishnan, R. Band gap engineering of amine functionalized Ag(I)-based coordination polymers and their plasmonic Ag^0 coupled novel visible light driven photo-redox system for selective oxidation of benzyl alcohol. *Appl. Catal. B Environ.* **2022**, *303*, 120821. [CrossRef]

53. Chen, K.; Wang, X.; Li, Q.; Feng, Y.N.; Chen, F.F.; Yu, Y. Spatial distribution of ZnIn$_2$S$_4$ nanosheets on g-C$_3$N$_4$ microtubes promotes photocatalytic CO$_2$ reduction. *Chem. Eng. J.* **2021**, *418*, 129476. [CrossRef]

54. Zhao, Y.; Deng, C.; Tang, D.; Ding, L.; Zhang, Y.; Sheng, H.; Ji, H.; Song, W.; Ma, W.; Chen, C.; et al. α-Fe$_2$O$_3$ as a versatile and efficient oxygen atom transfer catalyst in combination with H$_2$O as the oxygen source. *Nat. Catal.* **2021**, *4*, 684–691. [CrossRef]

55. Zhang, P.; Yang, M.; Han, D.; Liu, X.; Yu, X.; Xiong, J.; Li, Y.; Zhao, Z.; Liu, J.; Wei, Y. Activating well-defined α-Fe$_2$O$_3$ nanocatalysts by near-surface Mn atom functionality for auto-exhaust soot purification. *Appl. Catal. B Environ.* **2023**, *321*, 122077. [CrossRef]

56. Zhang, H.C.; Kang, Z.X.; Han, J.J.; Wang, P.; Fan, J.T.; Sheng, G.P. Photothermal Nanoconfinement Reactor: Boosting Chemical Reactivity with Locally High Temperature in a Confined Space. *Angew. Chem. Int. Ed.* **2022**, *61*, e202200093.

57. Wang, K.; Xing, Z.; Meng, D.; Zhang, S.; Li, Z.; Pan, K.; Zhou, W. Hollow MoSe$_2$@Bi$_2$S$_3$/CdS core-shell nanostructure as dual Z-scheme heterojunctions with enhanced full spectrum photocatalytic-photothermal performance. *Appl. Catal. B Environ.* **2021**, *281*, 119482. [CrossRef]

58. Christoforidis, K.C.; Montini, T.; Bontempi, E.; Zafeiratos, S.; Delgado Jaén, J.J.; Fornasiero, P. Synthesis and photocatalytic application of visible-light active β-Fe$_2$O$_3$/g-C$_3$N$_4$ hybrid nanocomposites. *Appl. Catal. B Environ.* **2016**, *187*, 171–180. [CrossRef]

59. Wu, S.; Hu, H.; Lin, Y.; Zhang, J.; Hu, Y. Visible light photocatalytic degradation of tetracycline over TiO$_2$. *Chem. Eng. J.* **2020**, *382*, 122842. [CrossRef]

60. Guo, J.; Wang, L.; Wei, X.; Alothman, Z.; Albaqami, M.; Malgras, V.; Yamauchi, Y.; Kang, Y.; Wang, M.; Guan, W.; et al. Direct Z-scheme CuInS$_2$/Bi$_2$MoO$_6$ heterostructure for enhanced photocatalytic degradation of tetracycline under visible light. *J. Hazard. Mater.* **2021**, *415*, 125591. [CrossRef] [PubMed]

61. Chen, Z.; Guo, H.; Liu, H.; Niu, C.; Huang, D.; Yang, Y.; Liang, C.; Li, L.; Li, J. Construction of dual S-scheme Ag$_2$CO$_3$/Bi$_4$O$_5$I$_2$/g-C$_3$N$_4$ heterostructure photocatalyst with enhanced visible-light photocatalytic degradation for tetracycline. *Chem. Eng. J.* **2022**, *438*, 135471. [CrossRef]

62. Hong, Y.; Li, C.; Yin, B.; Li, D.; Zhang, Z.; Mao, B.; Fan, W.; Gu, W.; Shi, W. Promoting visible-light-induced photocatalytic degradation of tetracycline by an efficient and stable beta-Bi_2O_3@g-C_3N_4 core/shell nanocomposite. *Chem. Eng. J.* **2018**, *338*, 137–146. [CrossRef]

63. Chen, Q.; Yang, W.; Zhu, J.; Fu, L.; Li, D.; Zhou, L. Enhanced visible light photocatalytic activity of g-C_3N_4 decorated ZrO_{2-x} nanotubes heterostructure for degradation of tetracycline hydrochloride. *J. Hazard. Mater.* **2020**, *384*, 121275. [CrossRef] [PubMed]

64. Xie, Z.; Feng, Y.; Wang, F.; Chen, D.; Zhang, Q.; Zeng, Y.; Lv, W.; Liu, G. Construction of carbon dots modified MoO_3/g-C_3N_4 Z-scheme photocatalyst with enhanced visible-light photocatalytic activity for the degradation of tetracycline. *Appl. Catal. B Environ.* **2018**, *229*, 96–104. [CrossRef]

65. Li, X.; Qiu, Y.; Zhu, Z.; Zhang, H.; Yin, D. Novel recyclable Z-scheme g-C_3N_4/carbon nanotubes/$Bi_{25}FeO_{40}$ heterostructure with enhanced visible-light photocatalytic performance towards tetracycline degradation. *Chem. Eng. J.* **2022**, *429*, 132130. [CrossRef]

66. Zhao, T.; Xing, Z.; Xiu, Z.; Li, Z.; Yang, S.; Zhou, W. Oxygen-doped MoS_2 nanospheres/CdS quantum dots/g-C_3N_4 nanosheets super-architectures for prolonged charge lifetime and enhanced visible-light-driven photocatalytic performance. *ACS Appl. Mater. Interfaces* **2019**, *11*, 7104–7111. [CrossRef] [PubMed]

67. Zhang, G.; Xu, Y.; Yan, D.; He, C.; Li, Y.; Ren, X.; Zhang, P.; Mi, H. Construction of k+ ion gradient in crystalline carbon nitride to accelerate exciton dissociation and charge separation for visible light H2 production. *ACS Catal.* **2021**, *11*, 6995–7005. [CrossRef]

68. Yavuz, C.; Erten-Ela, S. Solar light-responsive α-Fe_2O_3/CdS/g-C_3N_4 ternary photocatalyst for photocatalytic hydrogen production and photodegradation of methylene blue. *J. Alloys Compd.* **2022**, *908*, 164584. [CrossRef]

69. Li, Y.; Zhu, S.; Liang, Y.; Li, Z.; Wu, S.; Chang, C.; Luo, S.; Cui, Z. Synthesis of α-Fe_2O_3/g-C_3N_4 photocatalyst for high-efficiency water splitting under full light. *Mater. Des.* **2020**, *196*, 109191. [CrossRef]

70. Huang, W.; Li, Z.; Wu, C.; Zhang, H.; Sun, J.; Li, Q. Delaminating Ti_3C_2 MXene by blossom of $ZnIn_2S_4$ microflowers for noble-metal-free photocatalytic hydrogen production. *J. Mater. Sci. Technol.* **2022**, *120*, 89–98. [CrossRef]

71. Sun, M.; Zhou, Y.; Yu, T.; Wang, J. Synthesis of g-C_3N_4/WO_3-carbon microsphere composites for photocatalytic hydrogen production. *Int. J. Hydrogen Energy* **2022**, *47*, 10261–10276. [CrossRef]

72. Pan, J.; Dong, Z.; Wang, B.; Jiang, Z.; Zhao, C.; Wang, J.; Song, C.; Zheng, Y.; Li, C. The enhancement of photocatalytic hydrogen production via Ti^{3+} self-doping black TiO_2/g-C_3N_4 hollow core-shell nano-heterojunction. *Appl. Catal. B Environ.* **2019**, *242*, 92–99. [CrossRef]